

Elastic/Plastic Indentation Damage in Ceramics: The Lateral Crack System

D. B. MARSHALL,* B. R. LAWN,** and A. G. EVANS*

Department of Materials Science and Engineering, University of California, Berkeley, California 94720

The mechanics of lateral crack propagation in a sharp-indenter contact field are described. The driving force for fracture has its origin in the residual component of the elastic/plastic field, which becomes dominant as the indenter is unloaded. Expressions for equilibrium crack evolution are derived, with due allowance for the close proximity of crack plane and specimen free surface. As with the median/radial crack system considered in an earlier paper, the ratio hardness-to-modulus complements toughness in the fracture relations. The basic predictions of the theory are examined in terms of experimental measurements of lateral crack dimensions in materials with a wide range of mechanical properties. The prospects of predicting the extent of lateral fracture in other ceramics, and thence of establishing a base for analyzing such important practical properties as surface erosion, are discussed.

I. Introduction

THE fracture associated with elastic/plastic contact on brittle surfaces is of two basic types, "median/radial" and "lateral." An earlier study dealt with the first of these types.¹ Emphasis was placed on the role of deformation processes in driving the cracks: hardness H and stiffness E , in addition to toughness K_c , accordingly entered as controlling material parameters. All basic features of the median/radial crack evolution during the indentation cycle were found to be predictable by linear fracture mechanics analysis.

The intent of the present paper is to develop a similar analysis for the lateral crack system. Lateral cracks are observed to initiate near the base of the plastic deformation zone below the contact, and to spread out laterally on a plane closely parallel to the specimen surface.²⁻⁵ In a severe contact event these cracks can run to the surface to cause material removal. The first systematic observations of sharp-contact fracture, in glass,² showed that the lateral extension occurs during indenter unloading, in much the same way as the surface radials.¹ Subsequent work on other ceramics⁵ showed similar trends. Residual stresses were thereby identified as the primary driving force for lateral cracking. For want of a suitable theoretical model for handling this type of stress field, the lateral system has not hitherto been subjected to first-principles analysis—rather, semiempirical formula fits have been adopted for specific applications.⁵ In view of the key role played by lateral fracture in the erosion^{6,7} and wear^{8,9} of brittle surfaces, an attempt at a fundamental study would appear to be opportune.

The treatment presented here follows that of the median/radial analysis.¹ Thus, the elastic/plastic contact field is considered in terms of superposed elastic and residual crack driving forces. As with the median/radial system, the crack geometry is taken to be pennylike, but with the complication of an adjacent, parallel free surface. Again, only the crack propagation stage is considered.

Presented at the 83rd Annual Meeting, The American Ceramic Society, Washington, DC, May 6, 1981 (Basic Science Division No. 156-B-81). Received February 15, 1982; revised copy received May 20, 1982; approved May 26, 1982.

Supported by the U. S. Office of Naval Research under Grant No. N00014-81-K-0362 and by the Australian Research Grants Committee.

*Member, the American Ceramic Society.

**At the time this work was done, B. R. Lawn was on study leave from the University of New South Wales, New South Wales, Australia. He is now with the Fracture and Deformation Division, National Bureau of Standards, Washington, DC 20234.

II. Lateral Fracture Model

(1) Basic Description

Consider the idealized lateral crack system in Fig. 1. The contact at load P leads to a crack of characteristic radius c , at depth h below the surface. The plastic zone supports the indenter, included angle 2ψ (not shown), over the characteristic radius a , and extends outward to a radius b . At this point it is unnecessary to recognize the existence of the median/radial system in the construction of the model, even though this system precedes the expansion of the lateral crack in the contact cycle—crack interaction effects may be introduced more conveniently as a geometrical perturbation later in the analysis (Section II(2)). A similar statement may be made about the coexistence of more than one lateral crack (as commonly observed in more severe contact events⁶)—the model of Fig. 1 represents the growth of a primary lateral crack.

With the emphasis on crack propagation, details in the complex near field of the elastic/plastic contact do not need to be specified. The threshold conditions for lateral fracture are thereby excluded from the present analysis. It is nevertheless important to appreciate that a residual tensile stress develops at the nucleation center near the base of the deformation zone, so that a residual driving force P_r acts on the crack as the indenter is withdrawn (Fig. 1). In the absence of reversed plasticity within the central zone,¹ P_r reaches its maximum at full contact loading, and persists at this value on removal of the indenter. Thus, consistent with the procedure adopted in Ref. 1, the net mouth-opening force for the system may be expressed as the difference between an irreversible residual (opening) component and a reversible elastic (closing) component. Experimental observations indicate that lateral cracks initiate as the diminishing applied load approaches zero (Section III). Therefore the following analysis will be concerned only with the final unloaded configuration.

(2) Stress Intensity Factor

In accordance with the indentation fracture mechanics approach,³ a stress intensity factor is sought for the configuration of Fig. 1 in terms of contact load and crack size. It is not appropriate to use the standard formula for embedded pennylike cracks,¹ because of the presence of the specimen free surface. The importance of the free-surface influence may be inferred from the considerable uplift that is evident about the impression zone, as in Fig. 2;

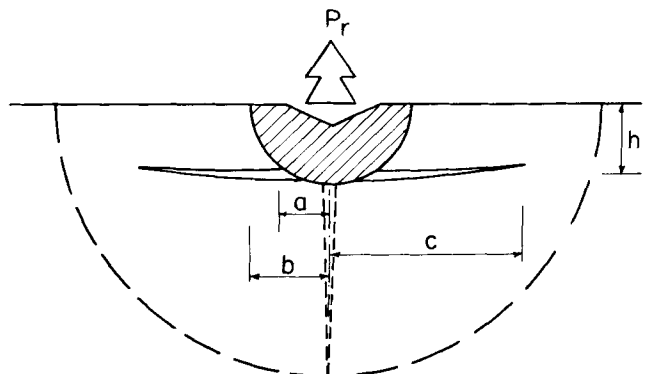


Fig. 1. Lateral crack system. Residual force, P_r , exerted by radially expanded plastic zone determines crack-driving force. Broken lines indicate median/radial crack system.



Fig. 2. Vickers indentation ($P=50$ N) in soda-lime glass; interference fringe micrograph, sodium light. Fringe distortion indicates surface uplift of material above lateral crack plane. Note distortion contained within bounds of radial crack traces (width of micrograph= $625 \mu\text{m}$).

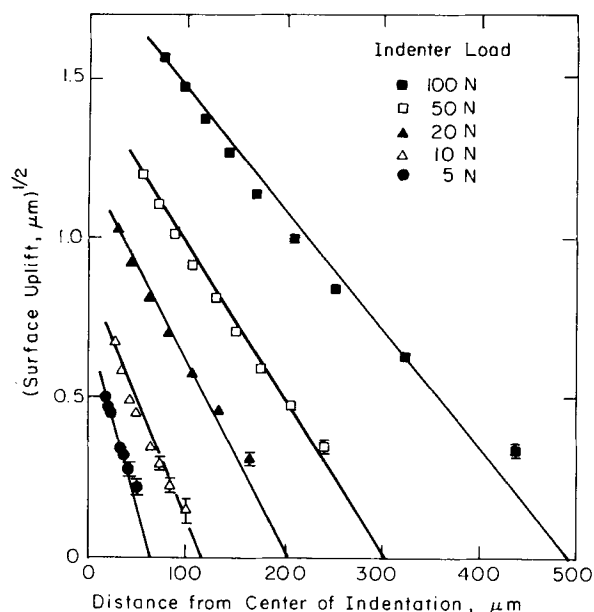


Fig. 3. Profiles of surfaces adjacent Vickers indentations in soda-lime glass. Measurements from optical interference micrographs; where error bars are not shown, measurement errors are smaller than data points.

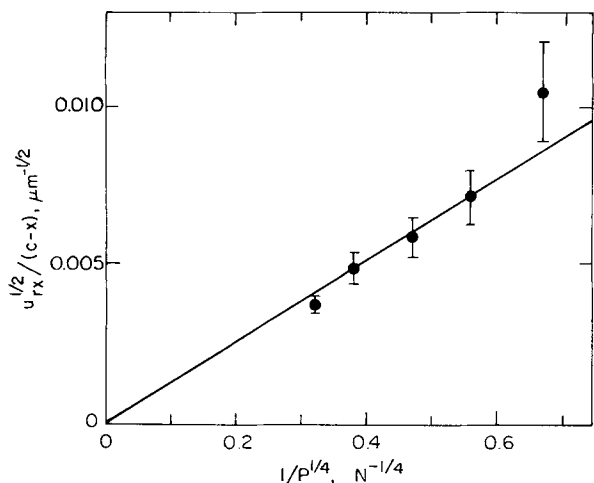


Fig. 4. Plot of measured (negative) gradients from Fig. 3 as a function of contact load parameter.

the disk of material above the crack plane is relatively free of bulk constraint, and must accordingly be expected to accommodate the greater proportion of the system's mechanical energy. No such uplift is observed around crack-free indentations. Close analogy between this configuration and that treated by Obreimoff¹⁰ (see, for example, Ch. 1 of Ref. 11) in his classical study of the cleavage of mica suggests that the lateral crack may be usefully modeled in terms of simple plate theory.¹² Conveniently, such an approach would be expected to be most accurate for $c \gg h$, i.e. in the requisite region of full crack propagation.

The analysis takes the material above the crack plane in Fig. 1 to be loaded elastically along its axis with force P_r and to be effectively "built-in" at radial distance c . The material below is much less compliant, and may therefore be treated as a rigid substrate. Then if u_r is the net load-point displacement at the disk center, a linear compliance relation of the form $u_r = \lambda P_r$ may be written for the crack system. A general displacement solution for a plate of Young's modulus E and Poisson's ratio ν loaded in this way is

$$\lambda = Ac^2/Eh^3 \tag{1}$$

where A is a dimensionless, geometrical constant. Detailed discussion of Eq. (1) is given in Appendix A, where two specific lateral/radial configurations are considered: (i) laterals \gg radials (full-plate approximation), giving $A = 3(1-\nu^2)/4\pi$; (ii) laterals $<$ radials (quarter-plate approximation), giving $A = 3/4$. The effect of preexistent radial cracks on lateral fracture mechanics is therefore accommodated by a simple adjustment in system compliance.

With the compliance thus determined, the crack extension force, G , follows directly from the standard formula (see Ch. 3 of Ref. 11)

$$G = (P_r^2/2)d\lambda/dC \tag{2}$$

where $C = \pi c^2$ is the crack area. Inserting Eq. (1) into Eq. (2), and making use of the equivalence relation $G = K^2(1-\nu^2)/E$ for plane strain fracture, the stress intensity factor is calculated as

$$K = [A/2\pi(1-\nu^2)]^{1/2} P_r/h^{3/2} \tag{3}$$

This result warrants special comment here. Noting that $[A/2\pi(1-\nu^2)]^{1/2}$ is a constant, the stress intensity factor is of the same form as that used for median/radial cracks,¹ but with the dimension h replacing c . The absence of any explicit term in crack length in Eq. (3) would appear to be inconsistent with the experimental observation that lateral cracks propagate in a highly stable manner. However, because of the relatively high compliance of the lateral system, it may be expected that the residual force P_r will relax significantly as propagation proceeds, thus making K a diminishing function of c . Specification of $P_r(c)$ accordingly becomes central to any fracture mechanics determination.

(3) Compliance Relation for Central Deformation Zone

It is now necessary to consider the mechanical characteristics of the central deformation zone. Recalling the sequence of operations used to evaluate the residual stress term in Ref. I (Section II(2A), Appendix A), it is expedient to adopt the analog of a precompressed linear spring. Then the residual force may be expressed as

$$P_r/P_{r0} = 1 - u_r/u_{r0} \tag{4}$$

$(0 \leq u_r \leq u_{r0})$

where P_{r0} is the force exerted by the spring element in the fully compressed state (i.e. at $u_r=0$) and u_{r0} is the displacement in the fully relaxed state ($P_r=0$). Since displacement is a much less accessible variable than load in contact testing, it is useful to use the linear compliance relation $u_r = \lambda P_r$ in conjunction with Eq. (1) to eliminate u_r from Eq. (4):

$$P_r = P_{r0}/(1 + AP_{r0}c^2/Eu_{r0}h^3) \tag{5}$$

The parameters P_{r0} , u_{r0} , and h provide the means for incorporating the elastic/plastic properties of the material into the formulation. To determine these parameters, expressions are first written for the characteristic dimensions of the plastic zone (Ref. 1,

Section II(2A)). For the residual impression, formed at peak indentation load P ,

$$a = (P/\alpha_0 H)^{1/2} \quad (6)$$

where H is defined as the hardness (invariant, in the approximation of geometrically similar indentations) and α_0 is a geometrical constant. For the elastic/plastic boundary,^{†,‡}

$$b = a(b/a) \sim (E/H)^{1/2} (\cot\psi)^{1/3} (P/H)^{1/2} \quad (7)$$

Now if $V \sim b^3$ is the volume of the zone and $\delta V \sim a^3 \cot\psi$ is the volume of the impression (Fig. 1), P_0 may be determined from the elastic/plastic mismatch stress, integrated over the zone cross-sectional area with no crack present,¹

$$P_0 \sim E(\delta V/V)b^2 \sim (E/H)^{1/2} (\cot\psi)^{2/3} P \quad (8)$$

whereas u_0 may be determined in terms of the radial displacement of the zone boundary, in going from the fully compressed to the fully relaxed state,

$$u_0 \sim \delta V/b^2 \sim [(H/E)/H^{1/2}] (\cot\psi)^{1/3} P^{1/2} \quad (9)$$

Finally, the thickness of the material above the crack plane may be identified with the depth of the plastic zone,⁶ so Eq. (7) gives

$$h \sim b \sim [(E/H)^{1/2}/H^{1/2}] (\cot\psi)^{1/3} P^{1/2} \quad (10)$$

It is noted that the parameters in Eqs. (8) to (10) increase with applied contact load, as intuitively expected.

(4) Equilibrium Fracture Mechanics Relations

An expression for the equilibrium crack size as a function of applied load is obtained by inserting Eqs. (5) and (8) to (10) into Eq. (3) and setting $K = K_c$:

$$c = c^L [1 - (P_0/P)^{1/4}]^{1/2} \quad (11)$$

where P_0 represents an "apparent threshold"[§]

$$P_0 = (\zeta_0/A^2) (\cot\psi)^{-2/3} (K_c^4/H^3)(E/H) \quad (12)$$

c^L represents a limiting crack function

$$c^L = \{(\zeta_L/A^{1/2}) (\cot\psi)^{5/6} [(E/H)^{3/4}/K_c H^{1/4}]\}^{1/2} P^{5/8} \quad (13)$$

and ζ_0 and ζ_L are dimensionless constants, independent of the material/indenter system. In the limit of large contact loads, $P \gg P_0$, Eq. (11) reduces to the simple power-law form, $c = c^L \propto P^{5/8}$, which accordingly represents a useful far-field approximation. Of special note here is the weak dependence of crack size on the compliance coefficient A , which indicates that lateral crack extension should not be strongly influenced by the preformed radial cracks.

III. Experimental Procedure

(1) Quantitative Verification of Compliance Model

A basic element of the model depicted in Fig. 1 is the relatively high compliance of the platelike material segment overlying the lateral crack. As indicated in reference to Fig. 2 earlier (Section II(2)), the readily apparent surface uplift in a region surrounding the impression zone is a direct manifestation of this compliance. To add further credence to the model, the surface displacements were measured quantitatively for soda-lime glass from the optical interference fringe patterns, and then analyzed in terms of the deflection geometry for simple plates in flexure.

To this end, it is noted from Fig. 2 that for Vickers indentations on soda-lime glass the lateral crack system conforms to the quarter-plate configuration. According to the analysis of Appendix A, the flexural profile for this configuration is circular with radius of

[†]Equation (7) represents an approximation to the elastic/plastic solution for an internally pressurized spherical cavity (Ref. 1, Appendix B). A more recent analysis (Ref. 13) indicates that $b/a \sim (E/H)^{2/5} (\cot\psi)^{1/3}$ provides a closer approximation for the indentation configuration. However, Eq. (7) has been retained in its present form in order to remain consistent with the radial crack analysis (Ref. 1) and because the small change in the exponent of (E/H) represents a minor modification to the equations that follow.

[‡]In the equations in this paper, the tilde (\sim) is used to indicate "varies as."

[§]This threshold is to be distinguished from that which pertains to crack initiation (Ref. 14), although it can be demonstrated that the critical loads have the same dependence on material parameters in the two cases (Ref. 15).

Table I. Parameters of Materials Studied

Material	E (GPa)	H (GPa)	H/E	K_c (MPa·m ^{1/2})
Soda-lime glass	70	5.5	0.08	0.75
MgF ₂ (HP)	120	6	.035	.6
ZnS (HP)	98	1.9	.02	.6
As ₂ S ₃ (glass)	16	1.4	.09	.23

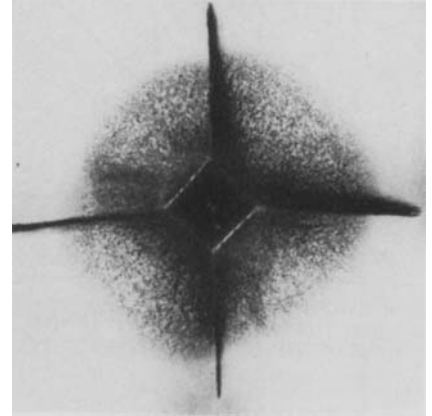


Fig. 5. Vickers indentation ($P=36$ N) in ZnS; reflected light, crossed polars (width of field=875 μ m).

curvature $R = 2Eh^3/3P$, = constant. It is then a matter of straightforward geometry to show that $(2Ru_{rx})^{1/2} = c - x$, where u_{rx} is the surface uplift at a distance x from the crack center. The square root of the measured surface uplift is accordingly plotted as a function of x for various selected contact loads in Fig. 3. Linear representations are obtained in each case by fixing the intercept on the abscissa at the observed lateral crack length and adjusting the slope to best fit the data. It will be noted that the gradients in Fig. 3 are dependent on load; this follows from the above formulas, in combination with Eqs. (8) and (10), from which gradient = $-u_{rx}^{1/2}/(c-x) \propto -1/R^{1/2} \propto -(P_r/Eh^3)^{1/2} \propto -1/P^{1/4}$ approximately. A plot of the negative of the gradients from Fig. 3 vs $P^{-1/4}$ does in fact appear to confirm the theoretically predicted trend, Fig. 4.

(2) Lateral Crack Measurements

The lateral cracking process was investigated for the group of materials listed in Table I. The materials were chosen to represent a wide range of mechanical properties, subject to the constraint that they be translucent.⁹ Thus, soda-lime glass, MgF₂, and ZnS provide variations in E/H (at approximately constant K_c) that extend over a range pertinent to most ceramics, whereas soda-lime and As₂S₃ glasses provide a significant variation in K_c at approximately constant E/H . Vickers indentations were made on polished surfaces in an oil environment. All measurements were taken within one minute of indenter removal in order to minimize the effects of moisture-assisted slow crack growth.**

(A) Preliminary Observations of Crack Evolution: Preliminary observations of lateral crack evolution were made using an indentation device which allowed in situ microscopic observation through a polished face normal to the indented surface. In all materials, the lateral cracks nucleated just prior to complete unloading of the indenter; crack formation involved an initial unstable propagation with subsequent arrest as the crack moved out of the near field, followed by stable propagation as the indenter unloading continued. The final crack length was always larger than $2a$. Figure 5, for ZnS, illustrates the typical crack pattern geome-

⁹Since lateral cracks are entirely subsurface, and sectioning techniques would be likely to modify the residual field (and, hence, the lateral crack configuration), reliable crack measurements are most simply obtained from materials that are at least partially transparent.

**Subcritical growth of lateral cracks is observed in an air environment (access of the environment to the subsurface cracks being provided, for example, by the residual opening of radial cracks). The oil environment reduces, but does not completely eliminate, slow crack growth.

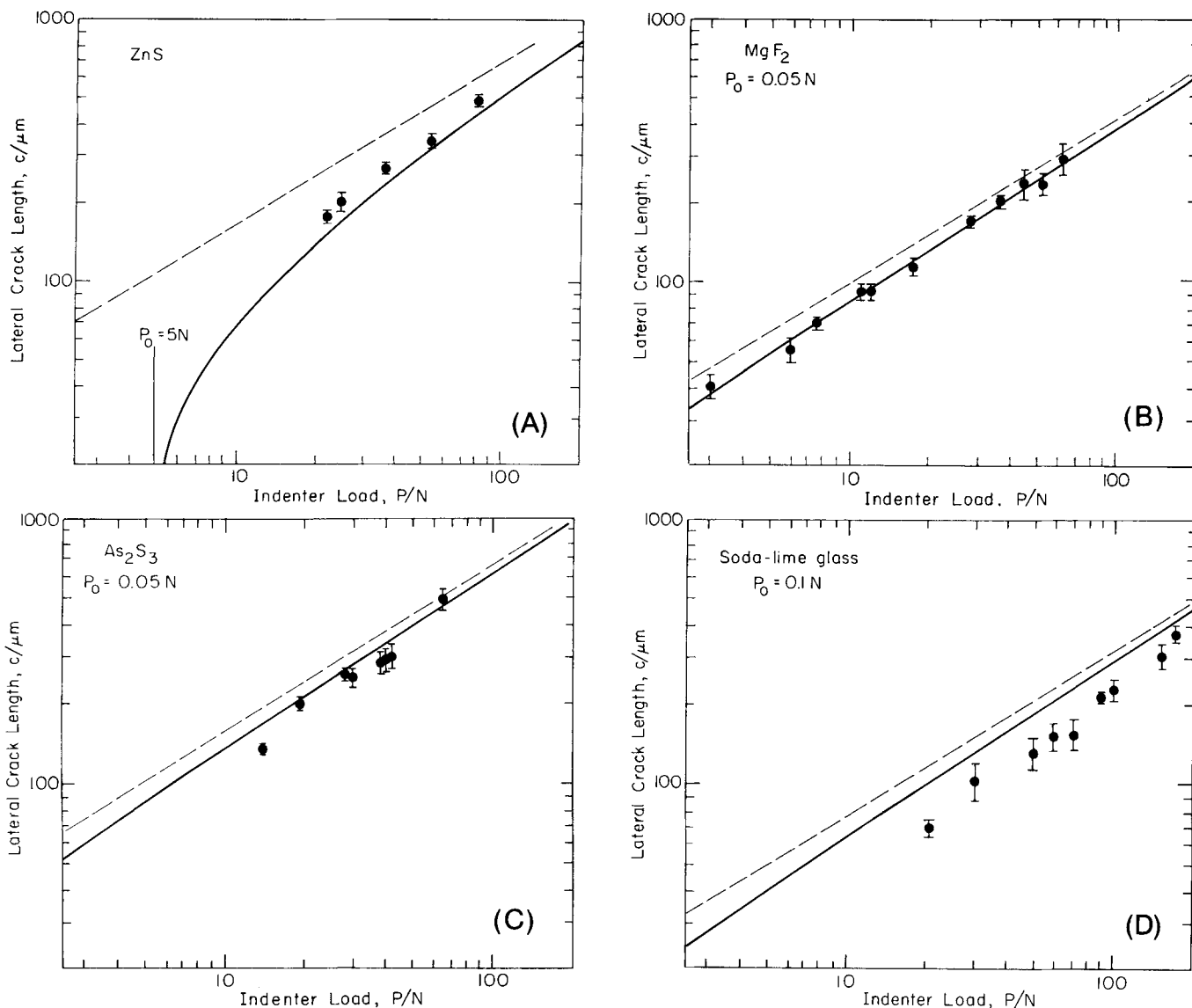


Fig. 6. Plot of lateral crack dimensions vs load for each material of Table I. Data points represent average of at least 4 measurements, with error bars representing standard deviation. Solid lines are predictions of Eqs. (11)–(13), with the dimensionless constants calibrated as described in Section III(2).

try. These observations are in accord with the earlier studies of soda-lime glass,² and confirm that the residual field provides the driving force for crack evolution. The peak indentation loads required for crack initiation varied between about 20 N for ZnS, 10 to 15 N for the soda-lime and As_2S_3 glasses, and less than 4 N for MgF_2 .^{††}

The depth below the indented surface at which lateral cracks formed showed considerable variability. The average depth was typically equal to the depth of the plastic zone (which could be distinguished with suitable illumination), although there was a systematic tendency for cracks in ZnS to form closer to the surface. Nevertheless, the ultimate crack length appeared to be relatively insensitive to the crack depth, so the relation $h \sim b$ (assumed in Section II) is used in the subsequent analysis.

(B) *Crack Dimensions:* Lateral crack dimensions were measured for each of the materials listed in Table I, from patterns such as that shown in Fig. 5, over as wide a range of indentation loads as practicable (limited at lower loads by initiation, and at the higher loads by chipping). The $c(P)$ data are plotted in Fig. 6. In all cases studied the radial cracks extended beyond the lateral cracks, so that the quarter-plate geometry ($A=3/4$) is appropriate.

The measurements were then analyzed in terms of the crack-size/indentation load relation, Eq. (11). It is noted from Eqs. (12) and (13) that there are two adjustable, dimensionless constants ζ_0 and ζ_L in Eq. (11). The object of the data analysis was to calibrate these two constants. This was done by least-squares fitting to all of the data points, taking $\psi=74^\circ$ (angle between pyramidal edges of Vickers indenter) and using the material parameters listed in Table I. The values thus obtained were $\zeta_0=1.2 \times 10^3$ and $\zeta_L=25 \times 10^{-3}$.

To test the calibration procedure, Eqs. (11) to (13) were used to regenerate the crack-size/indentation-load functions for each of the materials represented in Fig. 6. These functions are plotted as solid curves in the figure. Also included for comparison are the corresponding curves for the far-field approximation, $P_0=0$ (plotted as dashed lines).

IV. Discussion

(I) Analysis of Lateral Crack Model

The fracture mechanics analysis presented here establishes a basis for quantifying lateral crack growth in elastic/plastic contact fields. Central to the analysis is the dominance of the residual component of the field as a driving force for the crack system. The persistence of such a driving force after completion of the actual indentation event may manifest itself in continued, sub-

^{††}It is noted that crack nucleation can be strongly influenced by environmental moisture; at subthreshold indentation loads, cracks were observed to initiate up to 30 minutes after indenter removal, even in the relatively moisture-free oil environment.

critical extension of the lateral crack in moist environments (most sensitively reflected in the motion of interference fringe systems of the type shown in Fig. 2), leading in some cases to delayed surface chipping.

One of the more interesting aspects of the fracture mechanics analysis is the relation found between lateral crack size and indentation load. Whereas in the far-field approximation ($P \gg P_0$) this relation reduces to the power-law form $c \propto P^{5/8}$, for general load ranges the mathematical expression is considerably more complex. This is clear from Fig. 6(A), which shows the exact form of Eq. (11) to cut off at the apparent threshold load P_0 . Thus the gradient of any straight-line fit to a logarithmic plot of $c(P)$ data over a limited load range will generally be expected to be greater than $5/8$ by an amount which will decrease toward zero as P increases above P_0 . Of course, since the far-field solution always provides an overestimate of the crack size at a given indentation load, it may be used in conservative design where optimal resistance to surface damage is a prime specification.

The material requirements for maximum resistance to lateral fracture damage can be inferred from Eqs. (11) to (13). In the far-field region, where the crack length $c = c^L$ (corresponding to $P \gg P_0$) is given by Eq. (13), the material requirements are the same as for the radial crack system, viz. high values of K_c and H/E . The form of Eq. (13) was tested by calculating c^L for each set of indentation data in Fig. 6 (using Eq. (11)) along with values of P_0 calculated from Eq. (12) with the constant ζ_0 as calibrated in Section III(2(B)) and plotting $c^L/P^{5/8}$ for each material against $(E/H)^{3/4}/K_c^{1/2} H^{1/4}$ (Fig. 7). This plot confirms the predicted variation of c^L with material properties. The variation of cracking with material properties becomes considerably more complex for load ranges where the term P_0/P cannot be neglected in Eq. (11). There the requirements for minimal cracking are small c^L and large P_0 . These requirements are effected by high values of K_c . However, the influences of E and H on crack length become load-dependent because variation of either parameter provides opposing influences on crack length through the terms c^L and P_0 .

(2) Implications in Erosion Analysis

One of the most important consequences of lateral fracture is the role it plays in material removal processes such as solid particle erosion and abrasive wear. For erosion, the potential volume removal per impact event is (Fig. 1)

$$V_i \sim c^2 h \quad (14)$$

We have just indicated that for the detailed correlation of crack-length data with predictions of the lateral crack model, the term P_0/P in Eq. (11) should not be neglected. However, to obtain a conservative estimate of erosion volume under severe conditions we may neglect this term. Assuming the mean contact pressure during impact to be determined by the quasi-static hardness H in Eq. (6), the peak impulsive load is calculated as¹⁶

$$P \sim (H \tan^2 \psi)^{1/3} U_K^{2/3} \quad (15)$$

where U_K is the incident kinetic energy. Combination of Eqs. (10), (13), (14), and (15) then yields

$$V_i \sim \{(E/H)^{5/4}/K_c H^{1/6}\} U_K^{7/6} \quad (16)$$

as the erosion volume. This result is consistent with the observed velocity dependence of erosion data within the limits of experimental accuracy. However, most other theories of erosion predict similar velocity exponents,⁷ indicating that this aspect of the analysis is insensitive to details in the modeling. For instance, a theory based on a strictly dynamic contact with a spherical indenter of radius r , and which assumes the removal zone to be governed by radial crack dimensions, predicts^{6,17}

$$V_i \sim \{1/K_c^{4/3} H^{1/4}\} U_K^{19/12} / r^{13/12} \quad (17)$$

On the other hand, Eqs. (16) and (17) differ considerably in their dependence on material parameters, through the appearance of the elastic/plastic term E/H in the quasi-static prediction. Comparative tests on materials with similar values of toughness but widely different values of modulus-to-hardness may provide the

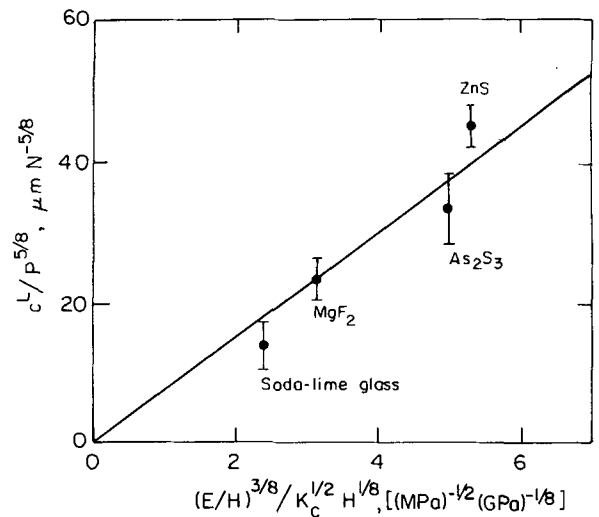


Fig. 7. Plot demonstrating correlation between load/crack-length parameter $(c^L/P^{5/8} = c/P^{5/8} [1 - (P_0/P)^{1/4}]^{1/2})$ and material properties, as predicted by Eq. (13). Data obtained from Fig. 6. Solid line represents Eq. (13).

means for distinguishing between alternative theories in different velocity regions.

Finally, it is acknowledged that the lateral crack model considered here will have certain limitations. Some have already been discussed in Ref. 1 in connection with the median/radial system: complications due to material densification or pile-up around the indenter and crack interaction effects (accommodated to some extent by the factor A in the present work) are pertinent examples. In addition, the mechanics of initiation has some bearing on the subsequent geometry of the fully developed lateral system: a variability of the depth of lateral cracking was noted in Section III and there is a tendency, most evident at high-load contacts, for multiple lateral cracking to occur.⁶ Further, the current model has not given explicit attention to the *path* of lateral fracture; deflection of the crack toward the surface as extension proceeds eventually causes chipping at high contact loads.

APPENDIX A

Elastic Plate Solutions for Lateral Crack System

The lateral crack configuration in Fig. 1 may be treated in terms of a center-loaded elastic plate with its outer edge clamped into a rigid matrix. Two particular cases, depending on the relative size of preceding radial cracks in the Vickers geometry, are dealt with here (Fig. A1):

(1) *Laterals extending beyond radials.* For this geometry the advancing crack front will experience relatively minor interactions with the radials, in which case the material above the lateral plane may be approximated by a circular plate. This geometry has the standard solution¹²

$$u_r/P_r = 3(1 - \nu^2)c^2/4\pi Eh^3 \quad (A-1)$$

(2) *Laterals contained within radials.* In this geometry the presence of the radials cannot be ignored. The lateral system may then be more usefully represented as a composite of four triangular quarter-plates, each right-angled at its apex where a force $P_r/4$ is acting. If Oxz defines the neutral surface of, say, the quarter-plate with axis Ox in Fig. A1, the plate compliance may be determined by considering a section at a distance x from the apex. The bending moment at x is then given as in simple beam theory by¹²

$$M_x = P_r x/4 \quad (A-2)$$

and the second moment of area for the (rectangular) section is

$$I_x = \omega h^3/6 \quad (A-3)$$

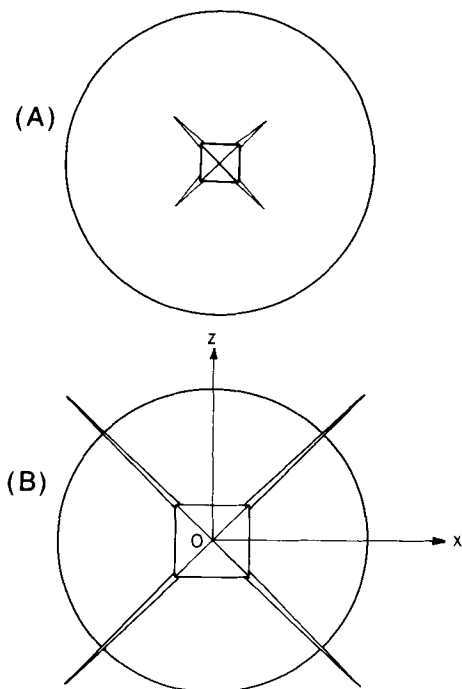


Fig. A1. Two possible lateral configurations with respect to preexisting radials in Vickers indentation, i.e. (A) laterals \gg radials and (B) laterals \ll radials.

where ω is the half-width and h the thickness. Noting that $\omega = x$ for a quarter-plate, the plate curvature at x becomes

$$R_x = EI_x/M_x = 2Eh^3/3P_r \quad (\text{A-4})$$

Now this quantity is independent of x , so the beam profile is circular, of radius $R = c^2/2u_r = \text{constant} = R_x$, from which

$$u_r/P_r = 3c^2/4Eh^3 \quad (\text{A-5})$$

References

- ¹B. R. Lawn, A. G. Evans, and D. B. Marshall, "Elastic/Plastic Indentation Damage in Ceramics: The Median/Radial Crack System," *J. Am. Ceram. Soc.*, **63** [9-10] 574-81 (1980).
- ²B. R. Lawn and M. V. Swain, "Microfracture Beneath Point Indentations in Brittle Solids," *J. Mater. Sci.*, **10** [1] 113-22 (1975).
- ³B. R. Lawn and T. R. Wilshaw, "Indentation Fracture: Principles and Applications," *J. Mater. Sci.*, **10** [6] 1049-81 (1975).
- ⁴B. J. Hockey and B. R. Lawn, "Electron Microscopy of Microcracking About Indentations in Aluminum Oxide and Silicon Carbide," *J. Mater. Sci.*, **10** [8] 1275-84 (1975).
- ⁵A. G. Evans and T. R. Wilshaw, "Quasi-Plastic Solid Particle Damage in Brittle Materials," *Acta Metall.*, **24**, 939-56 (1976).
- ⁶A. G. Evans, M. E. Gulden, and M. Rosenblatt, "Impact Damage in Brittle Materials in the Elastic/Plastic Response Regime," *Proc. R. Soc. London, Ser. A*, **361** [1706] 343-65 (1978).
- ⁷A. W. Ruff and S. M. Wiederhorn, "Erosion by Solid Particle Impact"; Ch. 2 in *Treatise on Materials Science and Technology: Vol. 16, Materials Erosion*. Edited by C. M. Preece. Academic Press, New York, 1979.
- ⁸B. R. Lawn, "A Model for the Wear of Brittle Solids Under Fixed Abrasion Conditions," *Wear*, **33**, 369-72 (1975).
- ⁹A. G. Evans, "Abrasive Wear in Ceramics: An Assessment," in *The Science of Ceramic Machining and Surface Finishing*. Edited by B. J. Hockey and R. W. Rice. *Symp. Proc., N. B. S. Spec. Publ.*, No. 562 (1979).
- ¹⁰J. W. Obreimoff, "The Splitting Strength of Mica," *Proc. R. Soc. London, Ser. A*, **127** [805] 290-97 (1930).
- ¹¹B. R. Lawn and T. R. Wilshaw, *Fracture of Brittle Solids*. Cambridge University Press, London, 1975.
- ¹²J. R. Roark, *Formulas for Stress and Strain*, Chs. 9 and 10. McGraw-Hill, New York, 1965.
- ¹³S. Chiang, D. B. Marshall, and A. G. Evans, "The Response of Solids to Elastic Plastic Indentation: I, "Stresses and Residual Stresses," *J. Appl. Phys.*, **53** [1] 298 (1982).
- ¹⁴B. R. Lawn and A. G. Evans, "A Model for Crack Initiation in Elastic/Plastic Indentation Fields," *J. Mater. Sci.*, **12** [11] 2195-99 (1977).
- ¹⁵B. J. Hockey, B. R. Lawn, and S. M. Wiederhorn, unpublished work.
- ¹⁶S. M. Wiederhorn and B. R. Lawn, "Strength Degradation of Glass Impacted With Sharp Particles: I, Annealed Surfaces," *J. Am. Ceram. Soc.*, **62** [1-2] 66-70 (1979).
- ¹⁷A. G. Evans, "Impact Damage Mechanics: Solid Projectiles"; Ch. 3 in *Treatise on Materials Science and Technology: Vol. 16, Materials Erosion*. Edited by C. M. Preece. Academic Press, New York, 1979.

Dependence of Fracture Toughness of Alumina on Grain Size and Test Technique

BERNHARD MUSSLER,* MICHAEL V. SWAIN,[†] and NILS CLAUSSEN*

Max-Planck-Institut für Metallforschung, Institut für Werkstoffwissenschaften, 7000 Stuttgart 80, Federal Republic of Germany

The fracture toughness (K_{Ic}) of sintered alumina was measured using notched beam (NB) and indentation/strength-in-bending (ISB) techniques. K_{Ic} (NB) decreases with increasing grain size. For fine-grained materials ($<5 \mu\text{m}$), NB results overestimate K_{Ic} and exhibit a substantial notch-radius sensitivity. A stress-intensity-derived model is used to explain this notch sensitivity. The ISB results are very similar to those obtained using the double-cantilever-beam (DCB) method and show an increasing fracture toughness with increasing grain size. The differences between the NB and ISB (DCB) results for coarser-grained materials are thought to be related to R -curve behavior.

I. Introduction

RECENTLY the present authors¹ summarized literature values of the grain-size dependence of the fracture toughness of alumina. The results were very confusing but some progress was made when the values were separated on the basis of test technique. The results of the notched-beam (NB) tests indicated that the fracture toughness increased with decreasing grain size, whereas the double-cantilever-beam (DCB) and work-of-fracture (WOF) tests show increasing toughness with increasing grain size to a maximum at $\approx 100 \mu\text{m}$. The latter results were confirmed by recent observations by Rice *et al.*² and are consistent with a theoretical model proposed by Rice and Freiman.³ The basis of their theoretical argument is that thermal-expansion-anisotropy (TEA) stresses

which develop on cooling from the fabrication temperature assist in the formation of intercrystalline microcracks about the advancing macrocrack and thereby increase the energy absorbed by the propagating crack.

From the observations reported¹ it appears that there are two areas of interest: small-grained microstructures ($<5 \mu\text{m}$) and materials with grain sizes $>10 \mu\text{m}$. In the intermediate range there is little difference in the reported values evaluated by the various test techniques of the fracture energy. Although much work has been done on the grain-size dependence of the fracture energy of alumina, most, with few exceptions, has not been over a sufficient grain-size range and may involve more than one preparation technique, e.g. sintering and hot-pressing.

The intent of this paper is to clarify the contradictory grain-size dependence of the fracture toughness of alumina as a result of test technique. Some of the comments as to these differences may also be applied to other materials for which other workers⁴ have observed large discrepancies between test techniques.

Received November 25, 1981; revised copy received April 14, 1982; approved April 19, 1982.

*Member, the American Ceramic Society.

[†]Now with Thomas J. Watson Research Center, IBM, Yorktown Heights, NY 10598.

¹On leave from CSIRO, Division of Materials Science, Advanced Materials Laboratory, Melbourne, Australia.